Elastic prestack reverse-time migration using a staggered-grid finite-difference method

Zaiming Jiang, John C. Bancroft, Laurence R. Lines, and Kevin W. Hall

ABSTRACT

Both staggered-grid finite-difference schemes and non-staggered schemes are popular in elastic wave modelling, while conventionally reverse-time migration is carried out through the non-staggered grid schemes. We present an elastic prestack reverse-time migration method using a staggered-grid finite-difference scheme.

The causes and characteristics of imaging artifacts of source-normalized imaging condition are analyzed. Based on this analysis, we practiced artifacts removal by subtracting neighborhood averages, by taking first derivatives, and by applying high pass filters.

The migration method is tested using a point diffractor model and a reduced set of the elastic Marmousi2 model.

INTRODUCTION

Finite-difference methods are practiced on numerical grid of nodal points both in space and time. Depending on the choice of the nodal points, the grid scheme can be classified in two broad categories: staggered and non-staggered. Seismologists use both schemes to simulate elastic wave phenomena.

The non-staggered grid scheme is widely employed in both modelling and migration of elastic waves. The early research began with modelling (Alterman and Karal, 1968; Alterman and Rotenberg, 1969; Alford, Kelly, and Boore, 1974; Kelly, Ward, Treitel, and Alford, 1976). Then this scheme is widely used in elastic reverse time migration since 1980's (Sun and McMechan, 1986; Chang and McMechan, 1987; Chang and McMechan, 1988; Sun and McMechan, 1988).

The staggered-grid scheme is also popular in the field of modelling. It became well known in modelling wave phenomena from two papers of Virieux (1984; 1986). Since then, the method has been developed from second-order to fourth-order (Levander, 1988) and then higher order, and from 2D to 3D (Ohminato and Chouet, 1997). It was shown that staggered-grid scheme deals with liquid-solid interface without the need for special treatment, which is not the case for non-staggered grid scheme (Virieux, 1986; Levander, 1988; Stephen, 1988).

Nevertheless, the staggered-grid scheme is rarely employed in reverse-time migration algorithms. The only document that I can find is by Wang (2000, PhD thesis). However, Wang's generally proposed algorithm needs both particle velocity and pressure data to be recorded, which is not practical.

This paper proposes an elastic prestack reverse time migration using a staggered-grid finite-difference method, in which only particle velocity surface record is needed for the

migration. In addition, based on interpreting the causes of imaging artifacts we give practical noise removal methods to improve the image obtained by normalized crosscorrelation imaging condition, which is one of the preferred imaging conditions (Chattopadhyay and McMechan, 2008).

MODELLING

Staggered-grid finite-difference method

The staggered-grid finite-difference method was developed by Virieux (1986), and we present a brief review of that work.

The elastodynamic equations

$$\rho\frac{\partial^2 u_x}{\partial t^2} = \frac{\partial \tau_{xx}}{\partial x} + \frac{\partial \tau_{xz}}{\partial z},$$

$$\rho\frac{\partial^2 u_z}{\partial t^2} = \frac{\partial \tau_{xz}}{\partial x} + \frac{\partial \tau_{zz}}{\partial z},$$

$$\tau_{xx} = (\lambda + 2\mu)\frac{\partial u_x}{\partial x} + \lambda\frac{\partial u_z}{\partial z}, \tag{1}$$

$$\tau_{zz} = (\lambda + 2\mu)\frac{\partial u_z}{\partial z} + \lambda\frac{\partial u_x}{\partial x},$$

$$\tau_{xz} = \mu\left(\frac{\partial u_x}{\partial z} + \frac{\partial u_z}{\partial x}\right)$$

can be transformed to the following system:

$$\frac{\partial v_x}{\partial t} = \frac{1}{\rho}\left(\frac{\partial \tau_{xx}}{\partial x} + \frac{\partial \tau_{xz}}{\partial z}\right),$$

$$\frac{\partial v_z}{\partial t} = \frac{1}{\rho}\left(\frac{\partial \tau_{xz}}{\partial x} + \frac{\partial \tau_{zz}}{\partial z}\right),$$

$$\frac{\partial \tau_{xx}}{\partial t} = (\lambda + 2\mu)\frac{\partial v_x}{\partial x} + \lambda\frac{\partial v_z}{\partial z}, \tag{2}$$

$$\frac{\partial \tau_{zz}}{\partial t} = (\lambda + 2\mu)\frac{\partial v_z}{\partial z} + \lambda\frac{\partial v_x}{\partial x},$$

$$\frac{\partial \tau_{xz}}{\partial t} = \mu\left(\frac{\partial v_x}{\partial z} + \frac{\partial v_z}{\partial x}\right)$$

where (u_x, u_z) is the displacement vector, $(\tau_{xx}, \tau_{zz}, \tau_{xz})$ is the stress tensor, $\rho(x,z)$ is the density, $\lambda(x,z)$ and $\mu(x,z)$ are the Lame coefficients, and (v_x, v_z) is the particle velocity vector.
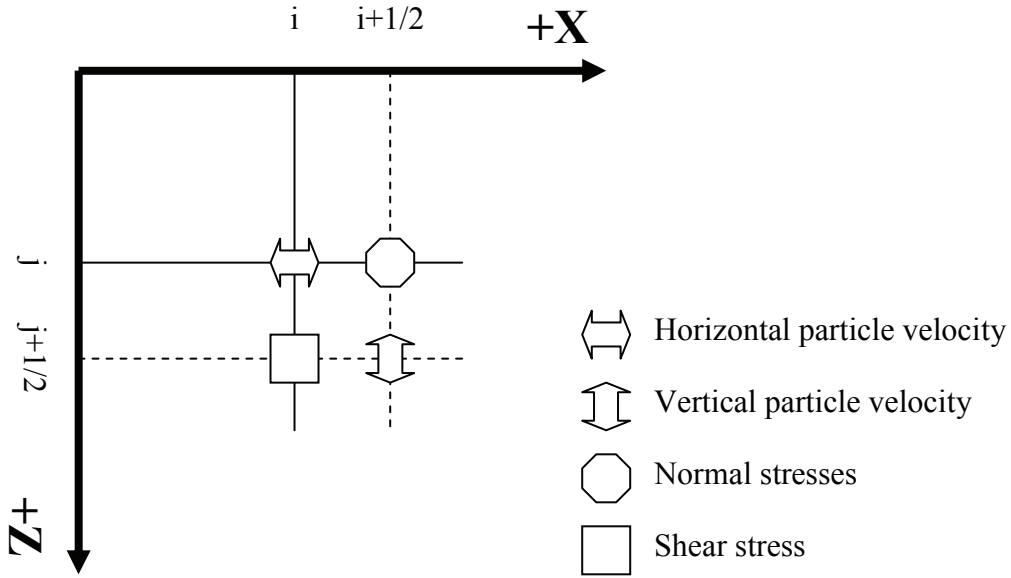
FIG. 1. Staggered finite-difference grid.

Discretizing the medium in the staggered-grid scheme shown in Figure 1, the system (2) can be derived as

$$U_{i,j}^{k+1/2} = U_{i,j}^{k-1/2} + B_{i,j}\frac{\Delta t}{\Delta x}(\Sigma_{i+1/2,j}^{k} - \Sigma_{i-1/2,j}^{k}) + B_{i,j}\frac{\Delta t}{\Delta z}(\Xi_{i,j+1/2}^{k} - \Xi_{i,j-1/2}^{k}),$$

$$V_{i+1/2,j+1/2}^{k+1/2} = V_{i+1/2,j+1/2}^{k-1/2} + B_{i+1/2,j+1/2}\frac{\Delta t}{\Delta x}(\Xi_{i+1,j+1/2}^{k} - \Xi_{i,j+1/2}^{k}) + B_{i+1/2,j+1/2}(\mathrm{T}_{i+1/2,j+1}^{k} - \mathrm{T}_{i+1/2,j}^{k}),$$

$$\Sigma_{i+1/2,j}^{k+1} = \Sigma_{i+1/2,j}^{k} + (L+2M)_{i+1/2,j}\frac{\Delta t}{\Delta x}(U_{i+1,j}^{k+1/2} - U_{i,j}^{k+1/2}) + L_{i+1/2,j}\frac{\Delta t}{\Delta z}(V_{i+1/2,j+1/2}^{k+1/2} - V_{i+1/2,j-1/2}^{k+1/2}),\tag{3}$$

$$\mathrm{T}_{i+1/2,j}^{k+1} = \mathrm{T}_{i+1/2,j}^{k} + (L+2M)_{i+1/2,j}\frac{\Delta t}{\Delta z}(V_{i+1/2,j+1/2}^{k+1/2} - V_{i+1/2,j-1/2}^{k+1/2}) + L_{i+1/2,j}\frac{\Delta t}{\Delta x}(U_{i+1,j}^{k+1/2} - U_{i,j}^{k+1/2}),$$

$$\Xi_{i,j+1/2}^{k+1} = \Xi_{i,j+1/2}^{k} + M_{i,j+1/2}\frac{\Delta t}{\Delta z}(U_{i+1,j}^{k+1/2} - U_{i,j}^{k+1/2}) + M_{i,j+1/2}\frac{\Delta t}{\Delta x}(V_{i+1/2,j+1/2}^{k+1/2} - V_{i-1/2,j+1/2}^{k+1/2})$$

where (i,j) is the space grid index, k is the time grid index, (U,V) is discretized (v_x,v_z), (Σ,T,Ξ) is discretized $(\tau_{xx},\tau_{zz},\tau_{xz})$, B represents buoyancy (the inverse of density), and L,M represent Lame coefficients.

The stability condition is

$$V_p\Delta t\sqrt{\frac{1}{\Delta x^2}+\frac{1}{\Delta z^2}} < 1,\tag{4}$$

which is independent of the S-wave velocity, or of the Poisson's ratio.

Source scheme

An explosive source was used. Four zero-phase Ricker wavelets were introduced into a staggered-grid model, with displacement directed uniformly about a centre. The peak

frequency of the Ricker wavelets is 40 Hz. Manning (2008) has successfully used this source scheme in his PhD thesis.
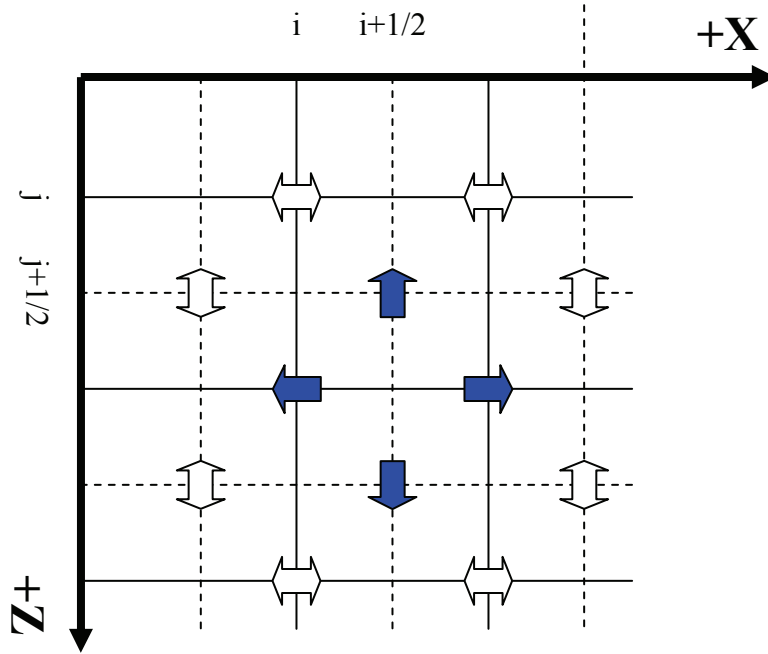

FIG. 2. An explosive source is simulated by four zero-phase Ricker wavelets.

Free surface boundary condition

Suppose that the boundary $z = 0$ is the Earth's surface. Then the boundary is a free surface, which means that the normal stresses must be zero at the surface. Thus,

$$\sigma_{xz} = \mu\left(\frac{\partial u_z}{\partial x} + \frac{\partial u_x}{\partial z}\right) = 0,$$

$$\sigma_{zz} = (\lambda + 2\mu)\frac{\partial u_z}{\partial z} + \lambda\frac{\partial u_x}{\partial x} = 0 \tag{5}$$

Take time difference, we get

$$\frac{\partial}{\partial t}\sigma_{xz} = \mu\left(\frac{\partial V}{\partial x} + \frac{\partial U}{\partial z}\right) = 0,$$

$$\frac{\partial}{\partial t}\sigma_{zz} = (\lambda + 2\mu)\frac{\partial V}{\partial z} + \lambda\frac{\partial U}{\partial x} = 0 \tag{6}$$

Applying central differencing on the second equation at the surface, we obtain

$$\mu_{i,-1/2}\left(\frac{V_{i+1/2,-1/2} - V_{i-1/2,-1/2}}{\Delta x} + \frac{U_{i,0} - U_{i,-1}}{\Delta z}\right) = 0$$

$$(\lambda_{i+1/2,0} + 2\mu_{i+1/2,0})\frac{V_{i+1/2,1/2} - V_{i+1/2,-1/2}}{\Delta z} + \lambda_{i+1/2,0}\frac{U_{i+1,0} - U_{i,0}}{\Delta x} = 0$$

(7)

Using these equations, we can calculate fictitious values of $V_{i+1/2,-1/2}$ and $U_{i,-1}$, which in turn, can be used to calculate stresses at the free surface at the next half time step.

Computational grid boundary condition

To reduce the artificial reflections that are introduce by the edge of the computational grid, a method combining the absorbing boundary conditions A1 (Clayton and Engquist, 1977) and the nonreflecting boundary condition (Cerjan, Kosloff, Kosloff, and Reshef, 1985) is applied to the sides and bottom of the subsurface model. The method of combining the absorbing and nonreflecting boundary conditions is demonstrated in another report "Combining absorbing and nonreflecting boundary conditions for elastic wave simulation".

Scatter point subsurface model

To illustrate both modelling and reverse time migration, a subsurface model contains a scatter point in a homogenous medium in $x - z$ plane is designed. The grid spacing is 2.31 m. The size of the scatter point is 11.55 m by 11.55 m. The time interval of modeling is 0.25 ms. Figure 3 shows the geometry and the P-wave velocities. The corresponding densities are calculated by Gardner's relationship; the corresponding S-wave velocities are calculated from P-wave velocities assuming Poisson's ratio is 0.25; then Lame coefficients are calculated from velocity and density parameters (Figure 4). Thus, we get the real subsurface model parameters used by the algorithm: densities and Lame coefficients.
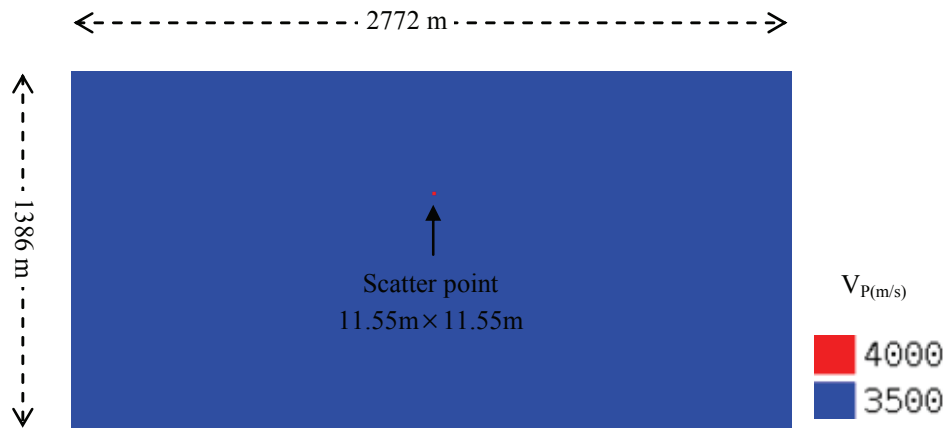

FIG. 3. A scatter point in a homogenous medium. This shows the P-wave velocities. S-wave velocities and densities are structured the same way.
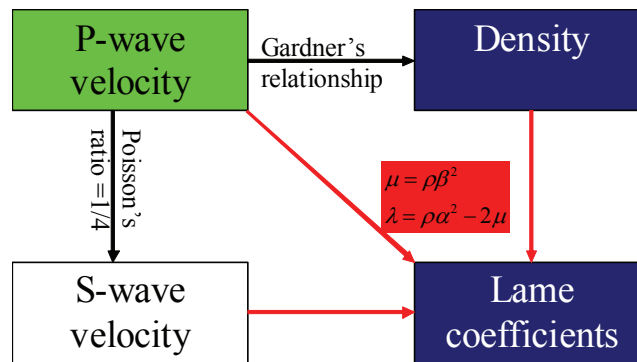
FIG. 4. Subsurface model parameters, densities and Lame coefficients, are calculated from P-wave velocities.

According to Huygens' principal, any modelling and migration algorithms which work properly on this scatter point subsurface model should work properly for any other models.

Centre shot vertical component snapshots are shown on the left column in Figure 5. (The middle and right column are, respectively, the reverse-time extrapolation snapshots and the crosscorrelation terms of the left and middle column. Further explanation is at the next section.) The wavefield contains P-wave, S-wave, and downgoing headwave. When the wave fronts (of the direct P-wave or S-wave) reach the scatter point, diffractions are produced since the wave length is bigger than the size of the point obstacle. When the reflected wave reaches the surface, it is recorded along with direct waves. Vertical component surface record of this shot is shown on the left in Figure 6.

REVERSE-TIME MIGRATION

"Reflectors exist at points in the ground where the first arrival of downgoing wave is time coincide with an upgoing wave" (Claerbout, 1971) . Retrieving the upgoing (reflected) wave from the surface record by reverse-time extrapolation and applying an imaging condition are the most important processes of reverse-time migration.

Reverse-time extrapolation

Reverse-time extrapolation is mostly the same processing as forward modelling: the same finite-differencing formulas and boundary conditions are used to do reverse-time extrapolation. Nevertheless, during this processing the surface record acts as numerous sources, and the process is reverse in time.

It is necessary to preprocess the surface record before it is used to do reverse-time extrapolation. The purpose of the extrapolation is to retrieve the upgoing (reflected) wave. Direct arrivals in the surface record have nothing to do with the reflected energy, so these should be removed from the surface record before the extrapolation by muting, as illustrated in Figure 6.

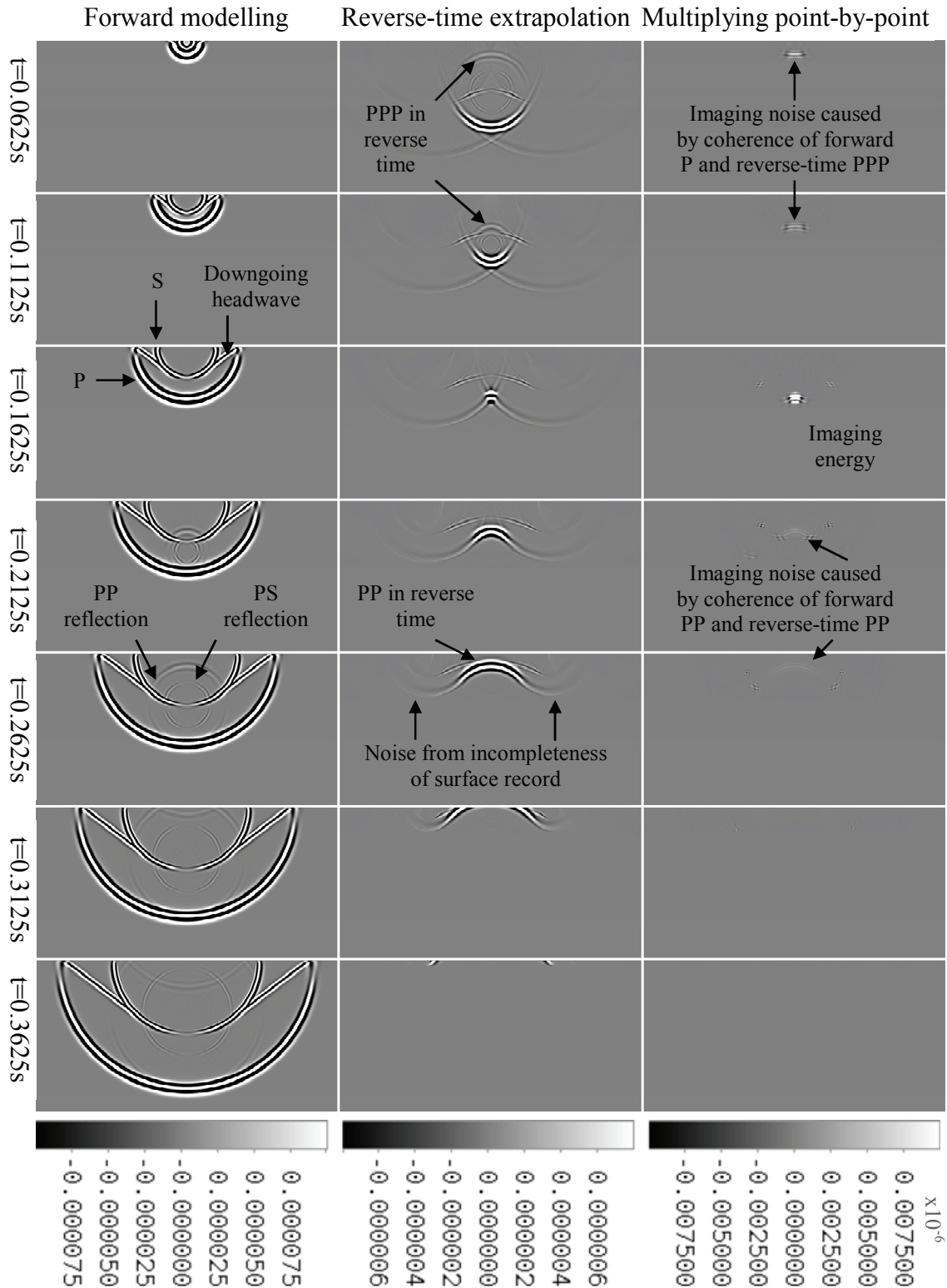Forward modelling   Reverse-time extrapolation Multiplying point-by-point

FIG. 5. Modelling and reverse-time extrapolation snapshots, and their multiplication point-by-point at seven different times. The left column is the modelling snapshots, which are calculated in time order; the middle column is the reverse-time extrapolation snapshots, which are calculated in reverse-time order; the right column is the crosscorrelation terms of the left and middle column.
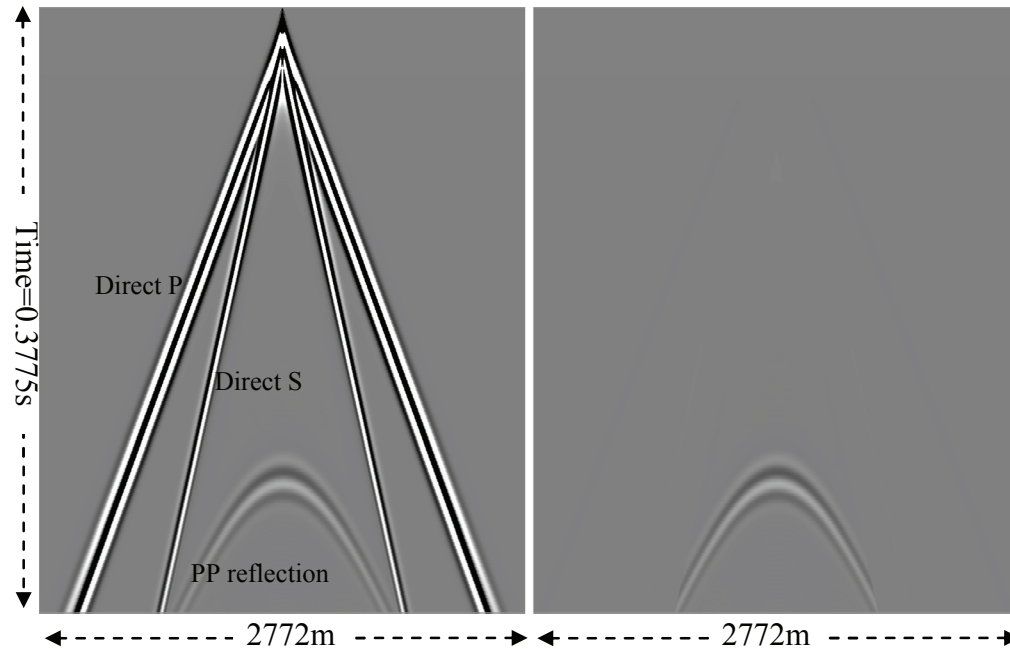
FIG. 6. Vertical component of the surface record of centre shot and the record after muting.

It is assumed that the medium is in equilibrium at the beginning of reverse-time extrapolation, i.e., initially stresses and particle velocities are set to zero everywhere in the medium. The assumption is usually not true since the time the extrapolation starts is the time the forward modelling of the incident wave stops, while at this time the subsurface wavefield usually exists. However, we have to follow the false assumption of zero initial condition, since the subsurface wavefield is unknown in a real seismic experiment. The false assumption of zero initial condition causes artifacts during the extrapolation. It also can be explained that the artifacts are caused by the incompleteness of surface record.

The middle column of Figure 5 shows the reverse-time extrapolation results of the centre shot. At time 0.3625 seconds the reflected PP wave starts showing up, as illustrated in the bottom of the middle column in Figure 5. In spite of the noise, the main energy, PP wave in reverse time, propagates towards the scatter point. Before the PP wave reaches the diffractor location, it is coincident with the reflected PP wave in the forward modelling. In fact, the PP wave in reverse time is extrapolated from the PP wave in forward modelling, except the part of extrapolation noise. After reaching the scatter point, the main part of reverse-time energy continues going down, but a small part is reflected up by the scatter point. We call this reflection PPP wave in reverse time. We can observe that the top-central part of the PPP-wave in reverse time is coincident with the bottom-central part of the direct P wave of the forward modelling.

Imaging condition

Normalized crosscorrelation imaging condition is one of the preferred methods for reverse-time migration (Chattopadhyay and McMechan, 2008). Source-normalized

crosscorrelation imaging condition is (Claerbout, 1971; Whitmore and Lines, 1986; Kaelin and Guitton, 2006; Chattopadhyay and McMechan, 2008)

$$image(x,z) = \frac{\sum_{time} S(x,z,t) R(x,z,t)}{\sum_{time} S^2(x,z,t)} ,$$ (8)

where $S(x,z,t)$ and $R(x,z,t)$ are, respectively, the source wavefield produced by modelling and the receiver wavefield produced by reverse-time extrapolation; $S(x,z,t)R(x,z,t)$ at certain time is interpreted as the coherence of the forward modelling wavefield and the reverse-time wavefield. Snapshots of $S(x,z,t)R(x,z,t)$ are shown on the right column in Figure 5.

Imaging artifacts

The imaging condition provides accurate estimates of reflection coefficients; however, it also leads to some artifacts. The most significant artifacts include two categories: artifacts below shot source and artifacts horizontally far away from shot source.

The artifacts below shot source (A1, as shown in Figure 7) are associated with reflectors below the shot source. There are two causes of the artifacts. The first cause is the coherence of the PP-wave in forward modelling and the PP-wave in reverse time, as shown at time 0.2625 seconds and time 0.2125 seconds in Figure 5; the second cause is the coherence of direct P-wave in forward modelling and PPP-wave in reverse time, as shown at time 0.1125 seconds and 0.0625 seconds in the same figure. These types of artifacts within the imaging result are shown in Figure 7. Suppose there are some other scatter points at the left and right side of the existing one, artifact A1 will be accumulated to a block of high imaging noise.

The artifacts horizontally far away from shot source (A2, as shown in Figure 8) associate with reflectors horizontally far away from the shot source. When the reflectors are horizontally far away from the point diffractor, they are exposed to the downgoing headwave and the S-wave. While the reflected PP-wave matches in reverse time, it coincident with the downgoing headwave and the S-wave in the forward modelling at certain times and certain locations, which leads imaging artifacts. These types of artifacts within the imaging result are shown in Figure 8. Suppose there are some point diffractors at the right side of the existing one, artifact A2 will develop into a block of high imaging noise.

The artifacts A2 are usually much stronger than the artifacts A1, as shown in Figure 7 and 8. This can be explained by the different causes of the artifacts. Suppose direct P-wave, S-wave, and downgoing headwave have the same amplitude x and the seismic-reflection coefficients of the reflector is 0.1, then reflected PP-wave has the amplitude of $0.1x$, and PPP-wave has the amplitude of $0.01x$. For artifacts A1, the product term $S(x,z,t)R(x,z,t)$, which is the product of PP-wave in forward modelling and the PP-wave in reverse time, or the product of direct P-wave in forward modelling and PPP-wave in reverse time, has the value of $0.01x^2$. While for artifacts A2, the product term, which is the product of downgoing headwave or direct S-wave in forward modelling and

the PP-wave in reserve time, has the value of $0.1x^2$, which is much higher than A1. The same observation result has been made by Kaelin and Guitton (2006): "Normalizing the cross-correlation by the source illumination for every shot reduces the artifacts close to the source, but it enhances the artifacts close to the receiver".

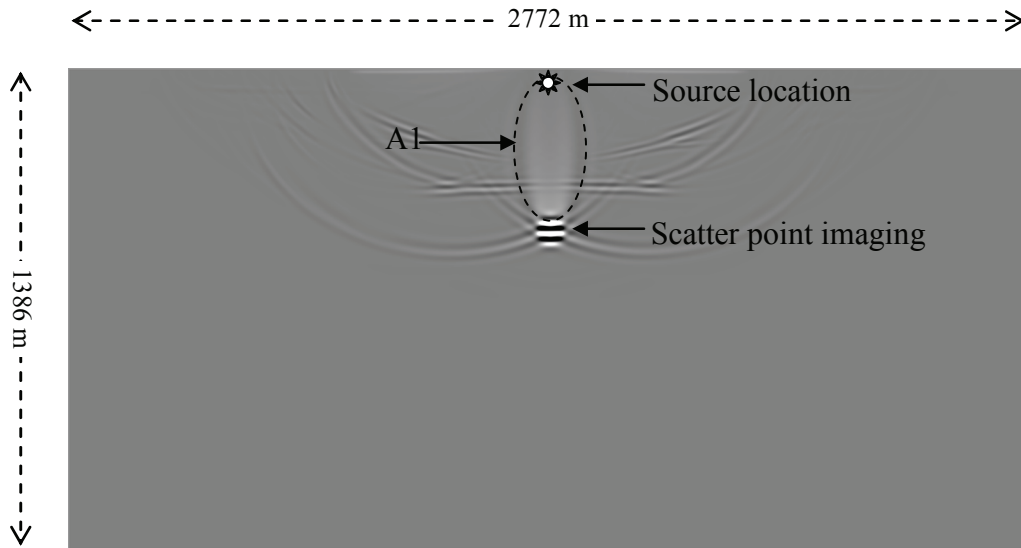Both artifacts are located above the reflector.

FIG. 7. Imaging result by applying source-normalized crosscorrelation imaging condition on centre shot for the subsurface model is shown in Figure 3. Artifact A1 is the most significant.
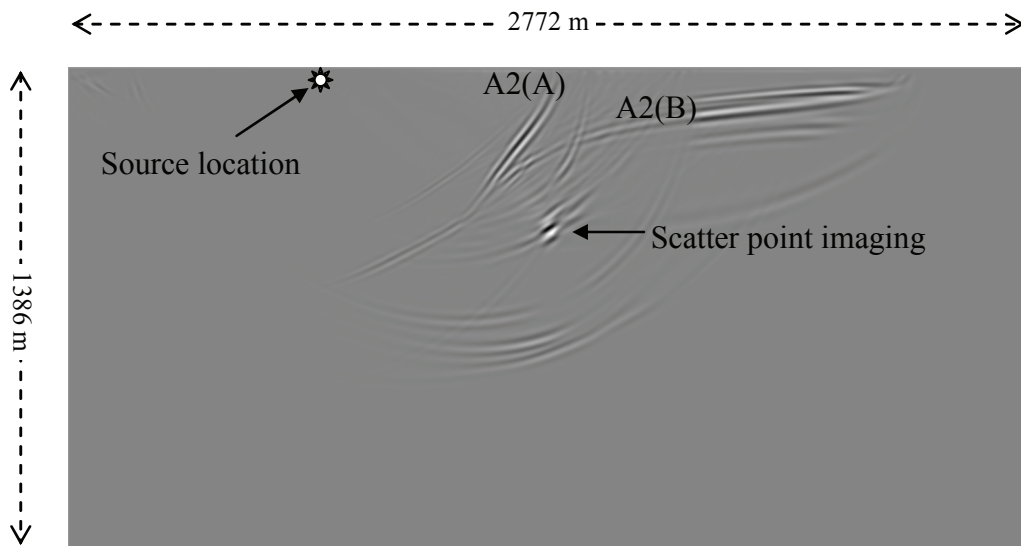
FIG. 8. When the source is horizontally far away from the point diffractor, there are strong imaging artifacts A2(A) and A2(B) produced by the normalized crosscorrelation imaging condition.

Stacking of shot images

After shot records are reverse-time migrated, the resulted shot images are stacked to obtain the subsurface image. Figure 9 shows the stacked image of 32 shots on the point diffractor subsurface model.

FIG. 9. Stacked image for point diffractor subsurface model. Totally 32 shot-images are stacked.

For a complex subsurface, there are numerous reflectors, while the shot records are far less in number. In this case, the imaging artifacts accumulate to very high levels. The following section will discuss about it.

PROCESSING OF MARMOUSI MODEL

New Marmousi model

The new Marmousi model used here is extracted from the elastic Marmousi2 model (Martin, 2004; Martin, Wiley, and Marfurt, 2006). First, the part from sample position (3201, 405) to (10560, 2800) of the Marmousi2 model is extracted to obtain the structure of the original acoustic Marmousi model. Then, we pick one node from every 3 nodes in x and z direction to obtain our down-sized Marmousi model. We develop this model to keep the complex structures of Marmousi2 model, but cut the size down, which has the advantage of less computational cost. Figure 10 shows the geometry of the new model and its P-wave velocities. The grid spacing is 1.25 m, the same as the Marmousi2.

To image the bottom corners of this model, the model is padded 1,000 m on the left side and 875 m on the right side. Then to apply nonreflecting boundary condition, the distance (or depth) of 312.5 m is padded on the sides and under the bottom.

Modelling of 64 shots is done, with the source interval being 70 m. The modelling time interval is 0.16 ms, and the total modelling time for each shot is 1.536 seconds. The top figure in Figure 11 shows the vertical component of one shot record, whose source is close to the centre on the surface. The surface record includes the padding on both sides,

and the values close to both sides are attenuated by applying the computational boundary conditions.
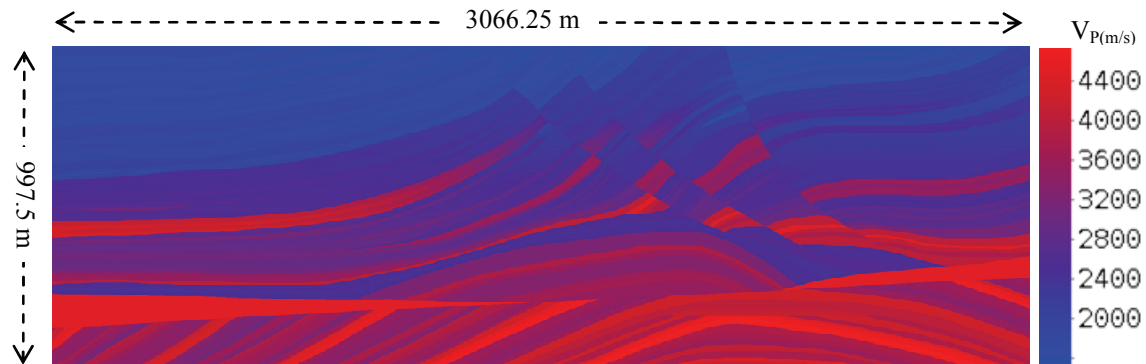

FIG 10. New Marmousi model extracted from the Marmousi2 model. It keeps the structure and elasticity of Marmousi2, but the size is much smaller.

Imaging and noise removal

The source-normalized imaging condition, equation (8), requires every snapshot of modelling to be stored in hard disk (instead of memory because of the large size) and then to be read to calculate the coherence with reverse-time extrapolated snapshots. To reduce computational cost, we use only one of every three snapshots. This is reasonable for this model, since it takes P-wave three time steps to travel the distance of one grid step.

Figure 11 shows the vertical component of one shot record, whose source is close to the centre on the surface, and the reverse-time depth migration result of this shot. The reverse-time depth imaging result includes the padding on both sides and bottom of the model.

Figure 12 shows the stacked image from the 64 shot images, which contains artifacts, and two traces from it. We can observe that the upper part values are higher than the lower part. This comes from the imaging artifacts. As described in the scatter point section, two types of significant artifacts, artifacts A1 and A2, are both above the reflector. If there are a lot of reflectors at different depth, the artifacts above them will accumulate more in the upper part of subsurface, which means higher crosscorrelation noise levels in the upper part. The crosscorrelation noise appears as low frequencies, or local DC biases, thus, the signals of reflectivity appear 'riding' on the low frequency artifacts. To obtain clear imaging result we need to remove the artifacts in the stacked image.
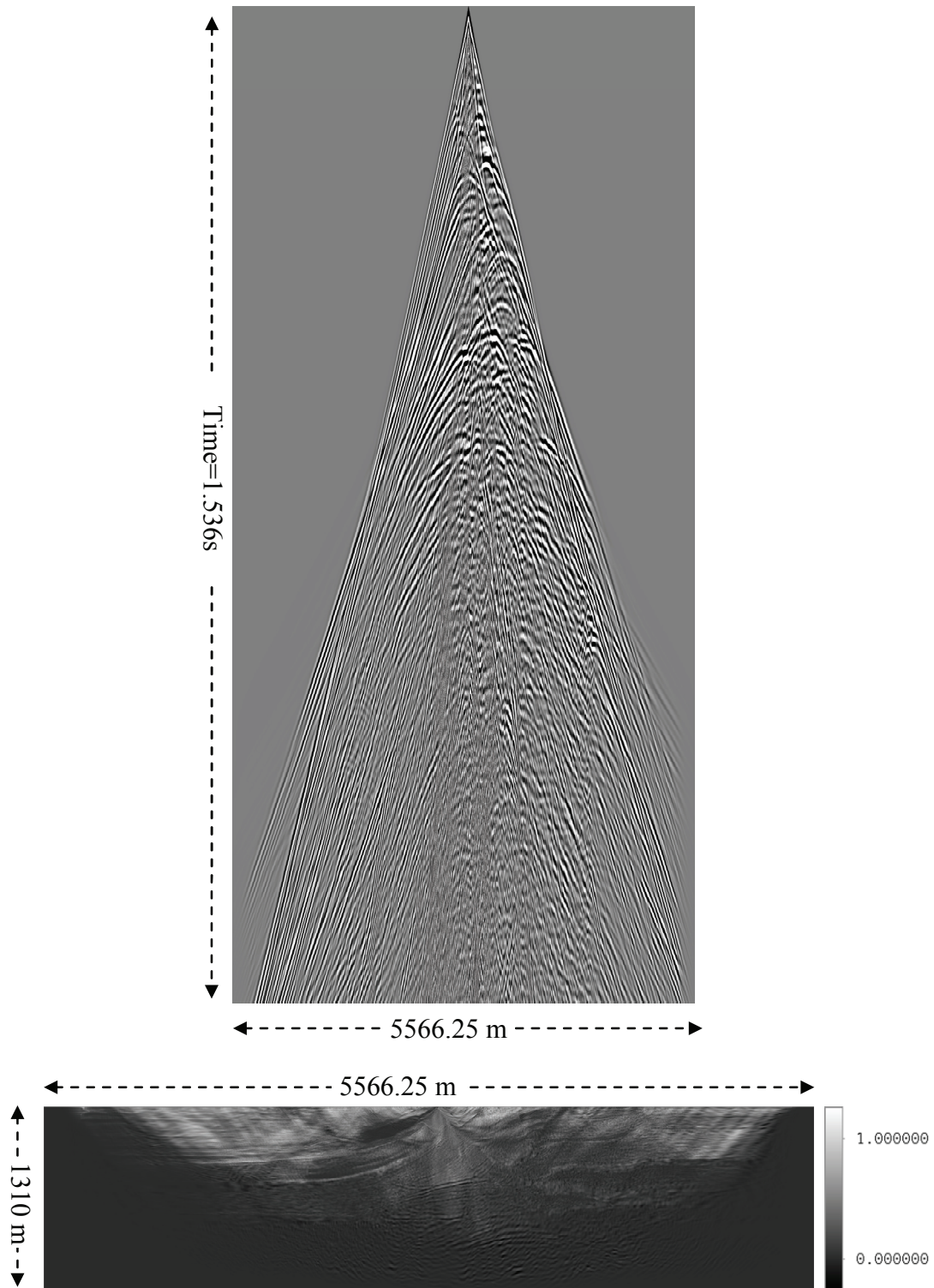
FIG. 11. The vertical component of one shot record (top), with the source being close to the surface centre, and the imaging result (bottom) of this shot by reverse-time depth migration.
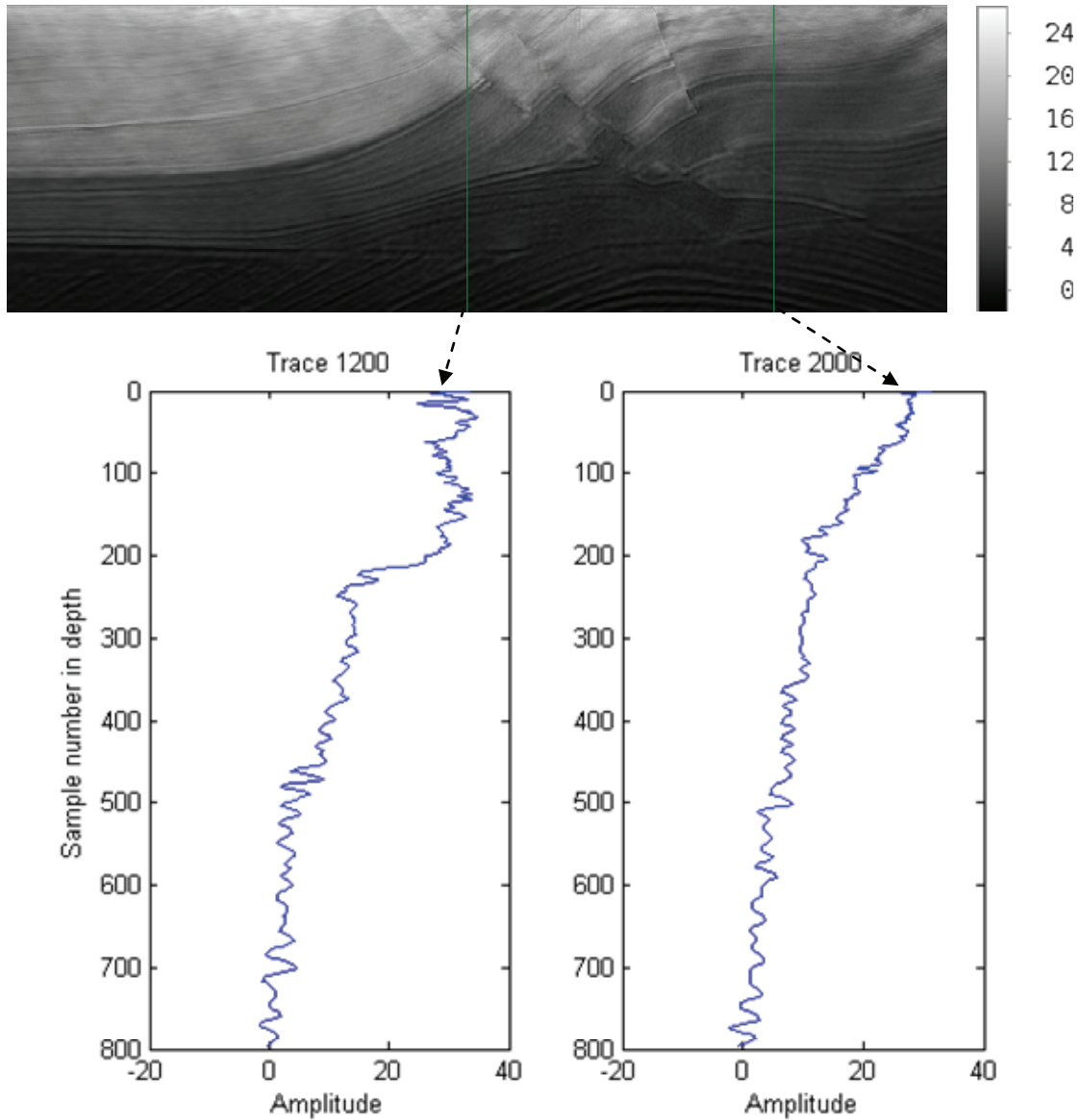
FIG. 12. The stacked image from 64 shot images and two traces from the stacked image.

We tried three methods to remove the low frequency artifacts, and the resulted images are shown in Figure 13.

The first method is subtracting neighborhood average values for each sample in the stacked image, since in a small window of neighborhood samples along the traces, the values appear like an AC signal rides on a DC bias. Along each trace of the data, for each sample, we define a certain length (50 samples) of window centered by this sample. We calculate the average amplitude of the samples in the defined window, and then this value is subtracted from the central sample value. In this way, each sample value is reduced by the neighborhood averages. The resulted image is shown on the top in Figure 13.
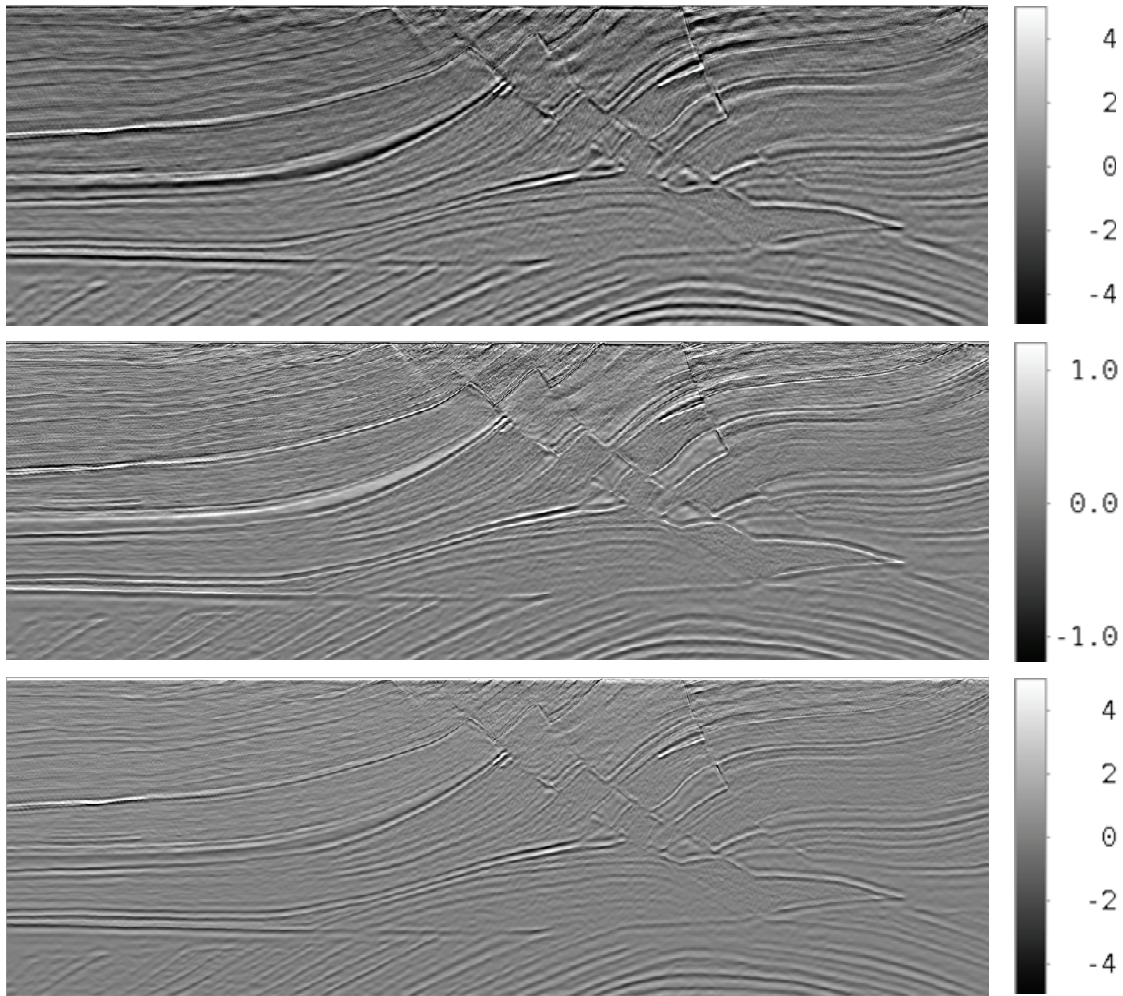
FIG. 13. Images resulted from different noise removal methods. The first image is the result of substracting neighborhood average values for each sample in the same traces. The second is the result of taking derivatives for each trace. The third is the result of using a high pass filter for each trace.

The second method is taking first derivatives along the traces in the stacked image. This method is often used within Kirchhoff migration (Bancroft, 2006). The resulted image is shown at the middle in Figure 13.

The third method is filtering the stacked image using a high pass filter since the artifacts are the low frequencies. The lowest frequency (actually wavenumber) of the signals is estimated, by counting wave circle numbers, as 0.028 wavenumber per metre from the traces shown on the bottom in Figure 12. Thus, the cutoff frequency for the high pass FIR filter is decided to be 0.026 wavenumber per metre.

Using MATLAB, we designed the filter, which is a Hamming-window based, linear phase, 48th order finite impulse response (FIR) filter. Because the normalized cutoff frequency 1.0 corresponds to the Nyquist frequency of 0.4 wavenumber per metre (since the grid spacing is 1.25 m), and the cutoff frequency is decided to be 0.026 wavenumber

per metre, the FIR filter's normalized cutoff frequency is set to $0.026 \div 0.4 = 0.065$ (Figure 14). Thus, the FIR filter coefficients are calculated in MATLAB as follows

$$h = \text{fir1}(48, 0.065, \text{'high'}). \tag{9}$$

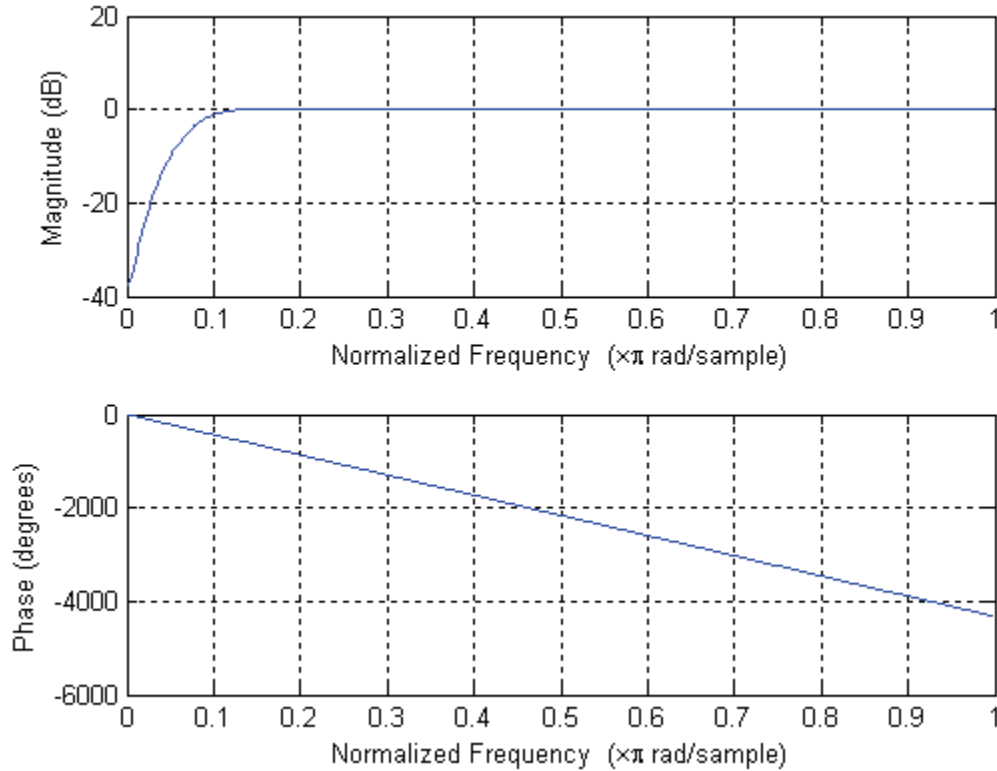

FIG. 14. Frequency response of the high pass FIR filter, which is used to filter the stacked image.

The resulted FIR filter coefficients are:

$$
\begin{aligned}
h(k) = \{&0.0010, 0.0012, 0.0013, 0.0016, 0.0018, 0.0020, 0.0019, 0.0016, \\
&0.0008, -0.0006, -0.0027, -0.0055, -0.0091, -0.0135, -0.0187, \\
&-0.0244, -0.0305, -0.0369, -0.0431, -0.0491, -0.0544, -0.0588, \\
&-0.0622, -0.0642, 0.9341, -0.0642, -0.0622, -0.0588, -0.0544, \\
&-0.0491, -0.0431, -0.0369, -0.0305, -0.0244, -0.0187, -0.0135, \\
&-0.0091, -0.0055, -0.0027, -0.0006, 0.0008, 0.0016, 0.0019, \\
&0.0020, 0.0018, 0.0016, 0.0013, 0.0012, 0.0010\}
\end{aligned}
\tag{10}
$$

where k is the index of the coefficients. Then the traces in the stacked image are filtered as follows

$$y(n - \frac{K}{2}) = \sum_{k=0}^{K-1} h(k)x(n-k), \qquad (11)$$

where x and y are, respectively, the input and output signals of the filter; n is the sample index in the trace; $K = 49$ is the length of filter; $\frac{K}{2}$ is the group delay of the FIR filter.

The filtered image is shown at the bottom in Figure 13. This result appears to be the best one.

CONCLUSIONS

We have presented an elastic prestack reverse-time migration method using staggered-grid scheme. This method is practical since only surface record of particle velocities, instead of both particle velocity and pressure data, is needed.

The source-normalized image condition leads to imaging artifacts because of (1) the coincidence of Direct P-wave in modelling and PPP-wave in reverse-time extrapolation, and (2) the coincidence of reflected PP-wave, Direct S-wave, and downgoing headwave in modelling and extrapolated PP-wave in reverse-time extrapolation. Imaging artifacts tends to accumulate more in shallow subsurface than in deep area, and they can be removed by subtracting neighborhood averages for each subsurface node, by taking first derivatives along the traces, or by applying a high pass filter along the traces.

ACKNOWLEDGEMENTS

REFERENCES

Alterman, Z.S., and Karal, F.C., 1968, Propagation of elastic waves in layered media by finite-difference methods: Bulletin of the Seismological Society of America, **58**, 367-398.

Alterman, Z.S., and Rotenberg A., 1969, Seismic wave in a quarter plane, bulletin of the Seismological Society of America, **59**, 347-368.

Alford, R.M., Kelly, K.R., and Boore D.M., 1974, Accuracy of finite-difference modeling of the acoustic wave equation, Geophysics, **39**, 834-842.

Bancroft, J.C., 2006, A practical understanding of pre- and poststack migration, Course notes.

Cerjan, C., Kosloff, D., Kosloff, R., and Reshef, M, 1985, A nonreflecting boundary condition for discrete acoustic and elastic wave equations, Geophysics, **50**, 705-708.

Chang, W.F., and McMechan, G.A., 1986, Reverse-time migration of offset vertical seismic profiling data using the excitation-time imaging condition: Geophysics, **51**, 67–84.

Chang,W.F., and McMechan, G.A., 1987, Elastic reverse-time migration, Geophysics, **52**, 1365-1375.

Chattopadhyay, S., and McMechan, G.A., 2008, Imaging conditions for prestack reverse-timemigration: Geophysics, **73**, no. 3, S81–S89.

Claerbout, J. F., 1971, Toward a unified theory of reflector mapping: Geophysics, **36**, 467–481.

Clayton, R., and Engquist, B., 1977, Absorbing boundary conditions for acoustic and elastic wave equations, bulletin of the Seismological Society of America, **67**, 1529-1540.

Clayton, R., and Engquist, B., 1980, Absorbing boundary conditions for wave-equations migration, Geophysics, **45**, 895-904.

Engquist, B. and Majda, A., Absorbing boundary conditions for numerical simulation of waves, Proc. Natl. Acad. Sci. USA, 74, 1765-1766.

Kaelin B., and Guitton A., 2006, Imaging condition for reverse time migration, SEG/New Orleans 2006 annual meeting, 2594-2598.

Kelly, K.R., Ward, R.W., Treitel, S., and Alford, R.M., 1976, Synthetic seismograms: a finite-difference approach, Geophysics, 41, 2-27.

Levander, A. R., 1988, Fourth-order finite-difference P-SV seismograms: Geophysics, **53**, 1425–1436.

Loewenthal, D., and Hu, L., 1991, Two methods for computing the imaging condition for common-shot prestack migration: Geophysics, **56**, 378–381.

Manning, P.M., 2008, Techniques to enhance the accuracy and efficiency of finite-difference modeling for the propagation of elastic waves, PhD thesis, University of Calgary.

Martin, G.S., 2004, The marmousi2 model, elastic synthetic data, and an analysis of imaging and AVO in a structurally complex environment, MSc thesis, University of Houston.

Martin, G.S., Wiley, R., and Marfurt, K.J., 2006, Marmousi2: An elastic upgrade for Marmousi, The leading Edge, February 2006, 156-166.

McMechan, G.A., 1983, Migration by extrapolation of time-dependent boundary values: Geophysical Prospecting, **31**, 413–420.

Ohminato T. and Chouet, B.A., 1997, A free-surface boundary condition for including 3D topography in the finite-difference method, Bulletin of the seismological society of America, **87**, 494-515.

Stephen, R.A., 1988, A review of finite difference methods for seismo-acoustic problems at the sea floor: Reviews of Geophysics, **26**, 445-458

Sun, R., and McMechan G.A., 1986, Pre-stack reverse-time migration for elastic waves with application to synthetic offset vertical seismic profiles, Proceedings of the IEEE, **74**, 457-465.

Sun, R., and McMechan G.A., 1988, nonlinear reverse-time inversion of elastic offset vertical seismic profile data, Geophysics, **53**, 1295-1302.

Virieux, J., 1984. SH wave propagation in heterogeneous media: velocity-stress finite-difference method, Geophysics, **49**, 1933--1957.

Virieux, J., 1986. P-SV wave propagation in heterogeneous media: velocity-stress finite-difference method, Geophysics, **51**, 889--901.

Wang Y., 2000, Variable grid-size and time-step finite difference method for seismic forward modeling and reverse-time migration, PhD thesis, University of Utah.

Whitmore, N.D., 1983, Iterative depth migration by backward time propagation: 53rd Annual International Meeting, SEG, Expanded Abstracts, 382–385.

Whitmore, N.D., and Lines, L.R., 1986, Vertical seismic profiling depth migration of a salt dome flank: Geophysics, **51**, 1087-1109.